7472 Vol. 57, No. 26 / 10 September 2018 / Applied Optics
Research Article

applied optics

Optimizing cirrus optical depth retrievals over the ocean from collocated CALIPSO and AMSR-E observations

Qiang Tang,[1,*] Yongxiang Hu,[2] Wei Li,[1] Jianping Huang,[3] and Knut Stamnes[1]

[1]Department of Physics, Stevens Institute of Technology, Hoboken, New Jersey 07030, USA
[2]NASA Langley Research Center, Hampton, Virginia 23681, USA
[3]College of Atmospheric Sciences, Lanzhou University, Lanzhou 730000, China
*Corresponding author: qtang@stevens.edu

Received 6 June 2018; revised 8 August 2018; accepted 9 August 2018; posted 9 August 2018 (Doc. ID 334557); published 5 September 2018

Retrievals of particulate optical depths and extinction coefficients from the cloud-aerosol lidar with orthogonal polarization (CALIOP) instrument deployed on the CALIPSO satellite mainly rely on a single global mean extinction-to-backscatter ratio, also known as the lidar ratio. However, the lidar ratio depends on the microphysical properties of particulates. An alternative approach is adopted to infer single-layer semi-transparent cirrus optical depths (CODs) over the open ocean that does not rely on an assumed lidar ratio. Instead, the COD is inferred directly from backscatter measurements obtained from the CALIOP lidar in conjunction with collocated sea surface wind speed data obtained from AMSR-E. This method is based on a Gram–Charlier ocean surface reflectance model relating wind-driven wave slope variances to sea surface wind speeds. To properly apply this method, the impact of multiple scattering between the sea surface and ice clouds should be taken into account. We take advantage of the 532 nm cross-polarization feature of CALIOP and introduce an empirical method based on the depolarization change at the sea surface to correct for potential bias in sea surface backscatter caused by whitecaps, bubbles, foam, and multiple scattering. After the correction, the COD can be derived for individual CALIOP retrievals in a single cloud layer over the ocean with this method. The global mean COD was found to be roughly 14% higher than the current values determined by the Version 4 CALIOP extinction retrieval algorithm. This study is relevant to future improvements of CALIOP operational products and is expected to lead to more accurate COD retrievals.

https://doi.org/10.1364/AO.57.007472

1. INTRODUCTION

Ice clouds (such as cirrus and contrails) are crucially important to radiative processes and the heat balance of Earth. They not only contribute to the distribution of absorbed solar radiation, but also control the energy emitted to space by Earth's system by modulating the thermal emission. Previous studies have shown that ice clouds affect the longwave radiation budget near the tropical tropopause [1,2], and the net global radiation is especially sensitive to the optical depth of high clouds, which consist mostly of ice crystals. Ice clouds have also been suggested to have a warming effect on the atmosphere [3,4]. All these radiative effects of ice clouds depend on their vertical structure and optical properties. The launch of CALIPSO provided vertical profiles of the atmosphere, measured by the active Cloud Aerosol Lidar with Orthogonal Polarization (CALIOP) instrument onboard CALIPSO [5]. These measurements represent a significant step toward a better understanding of ice cloud vertical structure, and this information can be used to improve estimation of cirrus temperature from satellite measurements and thereby enhance radiative transfer model predictions. However, accurate derivation of optical properties of semi-transparent ice clouds at visible wavelengths is still a significant challenge.

Ice cloud optical properties, such as extinction coefficient and optical depth, can be derived from either passive or active measurements. Passive sensors, such as the moderate resolution imaging spectroradiometer (MODIS) onboard the Aqua and Terra satellites, retrieve height-integrated cloud optical properties using shortwave and infrared radiances [6]. However, the non-sphericity of ice crystals, cloud multilayer structure, and the tendency for passive retrievals to be dominated by local radiation properties near the cloud top, make the retrieval of COD particularly challenging. The accuracy of the retrieval depends on the diversity of crystal sizes and shapes, and is very sensitive to ice crystal micro-physical assumptions [7]. Several investigators have shown that about 10% of clouds are missed by MODIS observations, and more than 20/10% of single-layer/multilayer cloud optical depths are underestimated by MODIS as compared with other active satellite measurements [8–10]. On the other hand, some active sensors, such as radars, underestimate particle size and are not very sensitive to small particles, implying that they may miss some semi-transparent ice clouds [11]. Other active sensors, such as elastic lidars, whether they are ground based or spaceborne [12–15], have difficulties, because lidar retrievals rely on an assumed extinction-to-backscatter ratio (also called the lidar ratio) and correction for multiple scattering to derive the optical depth from attenuated backscatter profiles.

To reduce the errors in lidar retrievals, attempts were made to benefit from the synergy provided by coincident observations from two different instruments [16–18]. For example, cirrus return signals may be used to calibrate lidar measurements [19], and accurate aerosol and cloud optical properties may be determined by use of collocated CloudSat cloud profiling radar (CPR) and CALIPSO lidar measurements [20,21]. Reagan and Zielinskie [22] developed a new algorithm to improve spaceborne lidar observations using lidar return signals from ground/sea reflections. Aerosol optical depths can be retrieved using this method from CALIPSO lidar ocean surface returns and an appropriate ocean surface reflectance model based on ocean surface wind speed [23,24].

To better understand the optical properties and global distribution of ice clouds without the lidar ratio assumption employed in conventional lidar retrievals, we have adopted an alternative way of deriving cirrus optical depth (COD) as well as cirrus lidar ratios. This approach takes advantage of synergistic A-train constellation CALIPSO and AQUA observations, with a temporal separation of 60–75 s and a perfect spatial collocation at the ocean surface. Based on the ocean surface backscatter signal from CALIOP and the ocean surface wind speed inferred from the AMSR-E instrument onboard AQUA, we optimize the approach of deriving accurate COD values as well as more reliable lidar ratios. Furthermore, we have attempted to effectively remove the multiply scattered signals at the sea surface using CALIOP cross-polarization measurements. To avoid any multilayer ice clouds in this study, we focus only on single-layer ice clouds with minimal aerosol loadings in the air. Hence, all multiple-layer cloud cases have been screened out using CALIOP Version 4 (V4) level-2 cloud layer data, and profiles with significant aerosol loadings are screened out by inspection of V4 level-2 aerosol layer data.

2. ANALYSIS AND METHODOLOGY

A. CALIOP Attenuated Backscatter Measurements

For an elastic backscatter lidar system such as CALIOP, the lidar equation [25,26] gives a relation between the received signal and the atmospheric backscatter, and the solution of the lidar equation can be used to retrieve profiles of particulate backscatter and extinction as follows:

$$\beta'(r) = \beta(r)T^2(r) \approx \frac{P(r)r^2}{CE}, \tag{1}$$

where $\beta'(r)$ (m^{-1} sr^{-1}) is the original attenuated backscatter coefficient, which is the main product of elastic lidar. $P(r)$ is the lidar signal received from a scattering volume at range r. The calibration factor C includes the amplifier gain, the transmitter–receiver overlap function, and losses in the transmitting and receiving optics. E is average laser output power. The volume backscatter coefficient $\beta(r)$ at range r, can typically be split into two terms: $\beta(r) = \beta_M(r) + \beta_P(r)$, with contributions from molecules (subscript M) and particulates (subscript P, including aerosols, water droplets, and ice particles). The two-way atmospheric transmittance $T^2(r)$ between the lidar and the scattering volume can be written as the product $T^2_{O_3}(r) \cdot T^2_M(r) \cdot T^2_P(r)$. The three parts of this product are:

1. the two-way transmittance due to absorption by ozone:

$$T^2_{O_3}(r) = \exp\left[-2\int_0^r \alpha_{O_3}(r')\mathrm{d}r'\right] = \exp[-2\tau_{O_3}],$$

where $\alpha_{O_3}(r')$ and τ_{O_3} are the ozone absorption coefficient and optical depth;

2. the two-way transmittance due to molecular scattering:

$$T^2_M(r) = \exp\left[-2\int_0^r \sigma_M(r')\mathrm{d}r'\right] = \exp\left[-2S_M\int_0^r \beta_M(r')\mathrm{d}r'\right] = \exp[-2\tau_M],$$

where $\sigma_M(r')$, S_M, and τ_M are the molecular scattering coefficient, the molecular extinction-to-backscatter ratio (the lidar ratio), and the molecular scattering optical depth, respectively;

3. the two-way transmittance due to attenuation by particulate matter:

$$T^2_P(r) = \exp\left[-2\eta\int_0^r \sigma_P(r')\mathrm{d}r'\right] = \exp\left[-2\eta_P S_P\int_0^r \beta_P(r')\mathrm{d}r'\right] = \exp[-2\eta_P\tau_P], \tag{2}$$

where η_P, $\sigma_P(r')$, S_P, and τ_P are the multiple-scattering factor, extinction coefficient, lidar ratio, and optical depth of particulates, respectively.

The attenuated backscatter coefficients $\beta'(r)$ are relatively easy to obtain from the raw lidar signal after calibration. For CALIOP, the nighttime signal at 532 nm in Version 3 (V3) data was calibrated by normalizing the observed signal to the predicted molecular signal obtained from the Global Modeling and Assimilation Office (GMAO) in the region between 30 and 34 km [27]. Recently, the accuracy of the 532 nm nighttime calibration in V4 data has been significantly improved by raising the calibration altitude from 30–34 km to a higher range of 36–39 km to ensure inclusion of the small yet significant contribution due to stratospheric aerosols. This procedure brings 2%–3% improvement of the calibration coefficients in V4 [28]. Both the 532 nm daytime calibration and the 1064 nm calibration benefit from the improved 532 nm nighttime calibration [29]. The daytime 532 nm calibration is obtained by interpolating the calibration constant between adjacent nighttime data. The 1064 nm calibration constant is determined by comparing the 1064 nm signals to the 532 nm signals from some properly selected target, such as high cirrus clouds. The calibration uncertainty is mainly due to the contribution from tiny aerosols in the stratosphere (at about the 1% level in V4) and random noise. However, retrieval of the more useful unattenuated particulate backscatter coefficient requires more information, such as the particulate lidar ratio, S_P. For CALIOP V3 data, the aerosol models and the particulate lidar ratios are based on a clustering analysis of AERONET data [30], and assessments show that on a global basis there are about 20%–30% uncertainty ranges for CALIPSO-modeled lidar ratios in V3 data [31–33], which could induce roughly 20%–30% underestimation of optical depth. Ice cloud lidar ratio and the multiple-scattering factor in V3 were fixed to a value of $25 \pm 10\ S_r$, and 0.6 been used in all ice cloud extinction retrievals.

In the most recent V4 data, ice cloud lidar ratios and multiple-scattering factors have been significantly improved [34] based on an extensive analysis of collocated measurements of V3 CALIOP cirrus optical depth and absorption optical depths retrieved from the CALIPSO infrared imaging radiometer (IIR) at 12.05 μm. Ice cloud multiple-scattering factors η_{cirrus} and lidar ratios S_{cirrus} are now approximated by a sigmoid function of the centroid temperature of cloud layers, where η_{cirrus} increases from a value of 0.46 at a centroid temperature of 0°C to 0.76 at −90°C; S_{cirrus} varies from 25 S_r at −70°C to 35 S_r at 0°C [35].

In this paper, we focus mainly on the backscatter signal from the open ocean surface. To reduce the error in determination of the lidar signal peak at the ocean surface due to sampling and sensor transient response, we consider the integrated attenuated ocean surface backscatter γ'_{att} (sr^{-1}) (performed 3 bins above and 1 bin below the ocean surface, each bin having a vertical resolution of 30 m), defined as

$$\gamma'_{\text{att}} = \int_{\text{base}}^{\text{top}} \beta'(r)\mathrm{d}r. \tag{3}$$

Here, γ'_{att} is due to 1) $\gamma'_{\text{ocean}} = \gamma_{\text{ocean}} T^2(r)$, the attenuated pure ocean surface backscatter, which is Fresnel backscatter from the wind-roughened ocean surface with two-way atmospheric attenuation, without any contamination from "junk" (such as whitecaps, bubbles, foams, etc.); and 2) $\gamma'_{\text{other}} = \gamma_{\text{other}} T^2(r)$, the "junk" backscatter due to the ocean subsurface, whitecaps, and bubbles [36,37] after attenuation. The contribution due to backscatter in part 2) can be effectively estimated from CALIOP depolarization measurements [36]. Thus, we have

$$\begin{aligned}\gamma'_{\text{att}} &= \gamma'_{\text{ocean}} + \gamma'_{\text{other}} \\ &= \gamma_{\text{ocean}} \exp[-2(\tau_{O_3} + \tau_M + \eta_P \tau_P)] + \gamma'_{\text{other}}.\end{aligned} \tag{4}$$

B. Ocean Surface Reflectance Model

Lidar backscatter from the ocean surface is closely related to the slope distribution of surface waves, which is commonly described by a statistical model in terms of surface roughness. An ocean surface reflectance model can be used to interpret lidar observations [36,38]. Based on linear wave theory, the sea-surface slopes can be assumed to have a Gaussian distribution, which for a non-isotropic Gaussian rough surface, can be written [39,40]

$$\begin{aligned} p(z'_x, z'_y) &= \frac{1}{2\pi\sigma_x\sigma_y} \exp\left[-\frac{1}{2}(\xi^2 + \eta^2)\right] \\ &= \frac{1}{2\pi\sigma_x\sigma_y} \exp\left[-\frac{1}{2}\left(\frac{z'^2_x}{\sigma_x^2} + \frac{z'^2_y}{\sigma_y^2}\right)\right], \end{aligned} \tag{5}$$

where ξ and η are the "standardized" slope component, which can be expressed as the ratio of the surface slope to the r.m.s. of the distribution, $\xi = \frac{z'_x}{\sigma_x}$ and $\eta = \frac{z'_y}{\sigma_y}$; z'_x, z'_y are the surface slopes for an anisotropic distribution in the upwind and crosswind directions; σ_x, σ_y are the standard deviation of the slopes in the upwind and crosswind directions, respectively.

Previous studies [41,42] have proven that when the (non-isotropic or isotropic) Gaussian probability distribution (PDF) was used, the model prediction was in good agreement with the measured data at the normal incidence angle, but it was in considerable disagreement when extended to angles away from normal incidence, implying that the slope distribution in the open ocean is not strictly Gaussian.

Cox and Munk [38] found that a more realistic Gram–Charlier expansion would fit the sea-slope PDF better through the observations of wave slopes from airborne photographs of sun glint. The Gram–Charlier distribution considers two additional factors compared with Gaussian distribution: peakedness and skewness, which leads to higher accuracy for small slopes. The Gram–Charlier PDF can be expressed as follows [38]:

$$p_{\text{GC}}(z'_x, z'_y) = p(z'_x, z'_y) \times \left(\begin{array}{c} 1 - \frac{1}{2}c_{21}(\xi^2 - 1)\eta - \frac{1}{6}c_{03}(\eta^3 - 3\eta) \\ + \frac{1}{24}c_{40}(\xi^4 - 6\xi^2 + 3) + \frac{1}{4}c_{22}(\xi^2 - 1)(\eta^2 - 1) \\ + \frac{1}{24}c_{04}(\eta^4 - 6\eta^2 + 3) \end{array} \right), \tag{6}$$

where c_{21} and c_{03} are skewness coefficients, and c_{40}, c_{22}, and c_{04} are peakedness coefficients. The terms after 1 in the big parentheses in Eq. (6) are the Gram–Charlier correction term. If skewness and peakedness are ignored ($c_{12} = c_{30} = c_{40} = c_{22} = c_{04} = 0$), Eq. (6) is reduced to the standard non-isotropic Gaussian distribution given by Eq. (5). Cox and Munk [38] determined these five coefficients as functions of wind speed for clean and slick water from sun glitter observations of the sea surface. However, the uncertainties in these coefficients obtained from Cox and Munk is about the same (or even higher) order of magnitude as the coefficients themselves [24,38].

A more complete form of the lidar equation that includes contributions from subsurface scattering has been proposed by Josset *et al.* [43]. Equation (21) in Ref. [43] takes into account specular reflectance, whitecap reflectance, and subsurface reflectance, and should be used if accurate measurements of ocean–air interface and whitecap coverage can be obtained. In our study, the contributions from whitecaps and subsurface scattering are empirically quantified by using the CALIOP depolarization technique [36]. Thus, we may use the Gram–Charlier distribution to approximate Eq. (21) in Ref. [43].

For an isotropic Gaussian slope distribution, $z'_x = z_x$, $z'_y = z_y$ and $\sigma_x = \sigma_y$, where z_x and z_y are the Gaussian surface slope components,

$$p(z_x, z_y) = \frac{1}{2\pi\sigma_x\sigma_y} \exp\left(-\frac{z_x^2 + z_y^2}{2\sigma_x^2}\right) = \frac{1}{\pi\sigma^2} \exp\left(-\frac{\tan^2\theta}{\sigma^2}\right), \quad (7)$$

where $\tan\theta = \sqrt{z_x^2 + z_y^2}$ is the isotropic surface slope, and $\sigma^2 = \sigma_x^2 + \sigma_y^2 = 2\sigma_x\sigma_y = 2\sigma_x^2 = 2\sigma_y^2$ is the variance of isotropic slope distribution.

The integrated sea surface backscatter, γ_{ocean} (sr^{-1}), for a nadir pointing system can be expressed based on Eq. (5) and Fresnel reflection as [36]

$$\gamma_{\text{ocean}} = \frac{\rho}{4\pi\sigma^2\cos^4\theta} \exp\left(-\frac{\tan^2\theta}{\sigma^2}\right), \quad (8)$$

where ρ is the Fresnel reflectance. However, the isotropic Gaussian slope distribution [Eq. (8)] ignores the effects of skewness and peakedness. It has been found that use of the Gaussian model would lead to an overestimation of the specular return from 13% to 11% for wind speeds between 1 and 10 m/s [24].

Furthermore, the Gram–Charlier correction term in Eq. (6) can be taken into account to fit CALIPSO observations [24]:

$$\gamma_{\text{ocean}} = \frac{\rho}{4\pi\sigma^2\cos^4\theta} \exp\left(-\frac{\tan^2\theta}{\sigma^2}\right)(1 + \Delta), \quad (9)$$

where Δ in Eq. (9) represents the Gram–Charlier correction term in Eq. (6). He *et al.* [24] used the collocated CALIOP and AMSR-E data between 23° and 40° in latitude in the southern hemisphere to obtain a polynomial fit of the Gram–Charlier correction term for CALIOP measurements. We will adopt this polynomial fit in our study, as well. The Δ term was shown to be a function of $\frac{1}{\sigma}$ as follows [24]:

$$\Delta\left(\frac{1}{\sigma}\right) = -0.0002\left(\frac{1}{\sigma}\right)^4 + 0.0076\left(\frac{1}{\sigma}\right)^3 - 0.1008\left(\frac{1}{\sigma}\right)^2 + 0.4780\left(\frac{1}{\sigma}\right) - 0.8232. \quad (10)$$

CALIPSO was pointed at 0.3° prior to 28 November 2007 to avoid specular reflections from calm waters and horizontally oriented ice crystals. The off-nadir angle was switched to 3° afterward to reduce the maximum values of integrated attenuated backscatter measured at both wavelengths, and to increase the minimum lidar ratios retrieved for strongly scattering ice clouds [5]. To make sure the specular reflection of the signal backscattered from the sea surface is received by a space-based lidar, the slope of the waves must be equal to the lidar incidence angle, θ_L. Hence, the pure ocean surface backscatter for CALIOP is obtained by

$$\gamma_{\text{ocean}} = \frac{\rho}{4\pi\sigma^2\cos^4\theta_L} \exp\left(-\frac{\tan^2\theta_L}{\sigma^2}\right)\left[1 + \Delta\left(\frac{1}{\sigma}\right)\right], \quad (11)$$

where $\rho \approx 0.0209$ for sea water at 532 nm and $\rho \approx 0.0193$ at 1064 nm for small angles of incidence.

Equation (11) provides a direct relation between the unattenuated sea surface backscatter and the variance of the slope distribution. From this equation we can get pure backscatter without attenuation from a wind-roughened ocean surface. As can be seen from Fig. 1, at small/moderate wind speeds

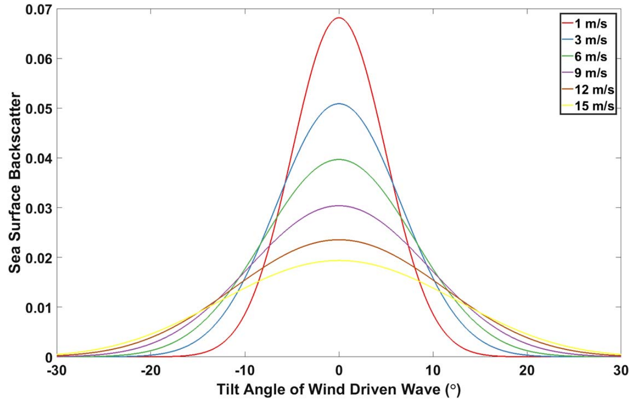

Fig. 1. Gram–Charlier relationship between sea surface backscatter and the slope of wind-driven waves at different wind speeds.

(red/blue/green curves), the slope of wind-driven waves varies in a small range. Thus, there is a good chance to get a large sea surface backscatter signal. As the wind speed increases (purple/brown/yellow curves), the wave slope varies in a larger range, and the corresponding sea surface backscatter signal is much smaller. Ideally the signal backscattered from the ocean surface will have the same polarization as the incident signal (no change in polarization state).

However, at high wind speeds ($U > 9$ m/s), the wind-driven waves start to break and form bubbles, whitecaps, and foam, and this situation leads to change in the polarization state of the backscatter signals. Hence, ocean surface backscatter will be contaminated by such "junk," as well as by ocean subsurface backscatter.

Another potential bias is due to multiple scattering at the ocean surface, which may lead to higher ocean surface backscatter and lower retrieved COD. Hence, the retrieved COD is accurate if the surface backscatter is from the laser beam that interacts with ocean surface only, ignoring possible interactions with ice clouds. In another words, the best situation is that the surface backscatter has no multiply scattered contribution from the overlying atmosphere, including ice clouds. However, due to surface roughness, there is a chance that the laser light is scattered by both ice clouds and the ocean surface before it is detected by the receiver. How severe can this multiple-scattering problem be? This fundamental question affects this method as well as its application to two new lidar missions such as the high spectral resolution lidar (HSRL) on board the EarthCARE satellite, to be launched in August 2019, and the differential absorption lidar (DIAL) on board the Merlin satellite, to be launched in December 2019. The potential biases due to multiple scattering is expected to increase with ice cloud and aerosol loadings.

To address this problem, we should take advantage of the cross-polarization feature of CALIOP and use the perpendicularly polarized signal of the ocean surface to help correct for it, since the multiply scattered ocean surface signals are expected to be perpendicularly polarized, while the singly scattered signal from the ocean surface is not. So, it is possible to reduce/eliminate the potential bias due to multiple scattering by removing the multiple-scattering contribution from the ocean surface backscatter. Based on Monte Carlo simulations, the contribution due to multiple scattering is roughly 4 times the perpendicular component of the ocean surface signal.

The overall contribution from "junk" and multiple scattering can be assessed from CALIOP real-time data and Monte Carlo simulations by using a lidar depolarization ratio of 15% [36]. At small wind speeds, the lidar depolarization ratio is close to 0. The subsurface backscatter can also be approximated by the depolarization technique. The total correction can be expressed as

$$\gamma'_{\text{other}} \approx \frac{\gamma'_{\text{ocean},\perp}}{0.15} + \gamma'_{\text{ocean},\perp} = 7.67\gamma'_{\text{ocean},\perp}, \tag{12}$$

where $\gamma'_{\text{ocean},\perp}$ is the measured attenuated perpendicular ocean surface backscatter for the CALIOP instrument. The correlation between AMSR-E wind speed and CALIOP lidar backscatter is almost doubled after this whitecap and subsurface correction [36].

C. U–σ^2 Relationship and Pure Integrated Ocean Surface Backscatter

The relationship between the wind speed U and the variance of the slope distribution $\boldsymbol{\sigma}^2$ has been the subject of many studies based on different measurements [36,38,44]. In 1954, Cox and Munk [38] first introduced a linear U–$\boldsymbol{\sigma}^2$ relation $\boldsymbol{\sigma}^2 = 0.003 + 0.00512U$ based on measurements of the bidirectional sea surface reflectance patterns of reflected sunlight. Wu [44] revised the linear relation to two log-linear relations using laboratory measurements. Hu *et al.* [36] refined the U–σ^2 relation into three segmented functions based on comparison between CALIPSO lidar sea surface backscatter and collocated AMSR-E wind speed measurements. The refined U–σ^2 relation based on CALIPSO–AMSR-E observations is given by [36]

$$\sigma^2 = \begin{cases} 0.0146\sqrt{U} & U < 7\ \text{m/s} \\ 0.003 + 0.00512U & 7\ \text{m/s} \le U < 13.3\ \text{m/s} \\ 0.138\log_{10} U - 0.084 & U \ge 13.3\ \text{m/s}. \end{cases} \tag{13}$$

From Eqs. (11) and (13), we can directly link the integrated sea surface backscatter γ_{ocean} with the sea surface wind speed U.

In this study, we take advantage of global sea surface wind speed measurements to obtain pure sea surface backscatter directly ("pure" indicates backscatter not contaminated by contributions from bubbles, whitecaps, and foam). Sea surface wind speeds have been widely observed from *in situ* platforms, such as ships [45], and space-based instruments, such as AMSR-E [46]. The AMSR-E wind speed product with a spatial resolution of about 20 km agrees well with other wind speed measurements [47,48].

Here we use the AMSR-E wind speed product to derive the pure integrated sea surface backscatter. Figure 2 shows the relationship between ocean surface wind speed and 1) ocean surface integrated backscatter and 2) slope variance of wind-driven waves. This figure explains the basic physics of the reflectance model. At small wind speeds, the slope of wind-driven waves is small and does not vary too much. The wave is flat and the corresponding backscatter is large. As the wind speed

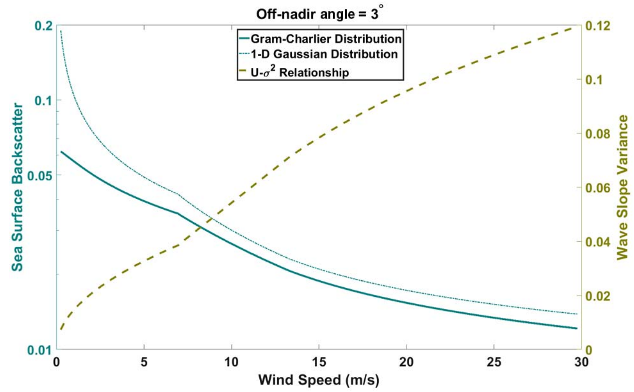

Fig. 2. Relationship between sea surface wind speed and (i) slope variance of wind-driven waves [right, Eq. (13)] and (ii) ocean surface integrated backscatter (left) based on two different surface reflection distributions: solid curve, Gram–Charlier distribution [Eq. (11)]; dashed–dotted curve, isotropic Gaussian distribution [Eq. (8)].

increases, the waves become steeper, the slope varies in a large range, and the corresponding backscatter becomes small.

D. Ice Cloud Optical Depth Retrievals

From Eq. (4), by using CALIOP lidar profiles for very clear atmospheric conditions (no water clouds, no aerosols, etc.), one can obtain the ice cloud optical depth as

$$\tau_P = \frac{1}{\eta_P}\left[-\frac{1}{2}\ln\left(\frac{\gamma'_{\text{att}} - \gamma'_{\text{other}}}{\gamma_{\text{ocean}}}\right) - \tau_M - \tau_{O_3}\right], \tag{14}$$

where γ_{ocean} can be derived from Eqs. (11) and (13) by using sea surface wind speed measurements. The multiple-scattering factor, η_P, introduced by Platt [49,50] is a convenient parameter to correct the apparent two-way transmittance for contribution from multiple scattering. Multiple-scattering effects in ice clouds are significant. In the CALIOP V4 algorithm, η_P is approximated by a sigmoid function of the centroid temperature of cloud layers, where η_P varies from 0.46 at a centroid temperature of 0°C to 0.76 at −90°C. We utilize this improved η_P in CALIOP V4 data to obtain the column optical depth. By doing so we avoid assuming an unrealistic value for η_P, and the results derived from our method can be better compared with CALIOP V4 cloud layer data with less uncertainty. Ozone and molecular optical depths, τ_{O_3} and τ_M, can be obtained from meteorological analyses produced by NASA's GMAO.

The ice cloud optical depth derived from this approach is a direct measurement, obtained without invoking any assumption about aerosol and cloud physical properties, such as the lidar ratio.

E. Lidar Ratio Retrievals from Ocean Surface Wind

For a given group of particles, the lidar ratio S_P (sr) is defined as the ratio of the extinction coefficient σ (m^{-1}) to the backscatter coefficient β (m^{-1} sr^{-1}). For CALIPSO, the particulate lidar ratio is based on cluster analysis of the ground-based AERONET dataset, and CALIPSO fixed the lidar ratio for different aerosol or cloud types. For atmospheric conditions in which molecular scattering is negligible compared to scattering by large particles, $T^2(r) \approx T_P^2(r)$, the lidar ratio can be obtained directly from the basic lidar equation [25].

From Eq. (2), by differentiating $T_P^2(r)$ and combining the result with Eq. (1), we obtain a first-order differential equation:

$$\frac{dT_P^2(r)}{dr} = -2\eta S_p \beta'(r).$$

For a range r^*, if the two-way transmittance $T_P^2(r^*)$ is known, the particulate lidar ratio S_P can be easily derived by solving the above equation to obtain

$$S_P = \frac{1 - T_P^2(r^*)}{2\eta\gamma'_{r^*}}, \tag{15}$$

where $\gamma'_{r^*} = \int_0^{r^*} \beta'(r)\mathrm{d}r$ is the column-integrated attenuated backscatter.

In this study, we can obtain S_P if $T^2(r^*)$ can be accurately estimated from Eq. (4) by using the ocean surface as a target. The retrieved lidar ratio can be used instead of the approximate value used in the CALIPSO extinction algorithm. It can also be applied to any other elastic lidar system.

Figures 3 and 4 show the feasibility of deriving 532 nm ice cloud lidar ratios from our ocean surface reflection method (OSRM) at both daytime and nighttime. The lidar ratios are rather stable throughout the optical depth of ice clouds. At small optical depth τ close to 0.5, the ice clouds are very thin, and the retrieved lidar ratios have stable values with small variations, which are mainly due to temperature and latitude dependence [34]. The zonal mean lidar ratios at both daytime and nighttime are given in the lower panels of Figs. 3 and 4. The hump of the nighttime lidar ratios around 15°S–20°S may indicate "warmer" ice clouds found in those areas.

The mean 532 nm cirrus lidar ratio derived from OSRM is 33.8 ± 4.9 sr for daytime, 35.3 ± 4.7 sr for nighttime, and the corresponding mean lidar ratios from CALIOP V4 data are 31.8 ± 4.7 sr for daytime and 32.7 ± 4.3 sr for nighttime. The lidar ratio for semitransparent cirrus was suggested by other authors [21,35] to be rather stable over the ocean

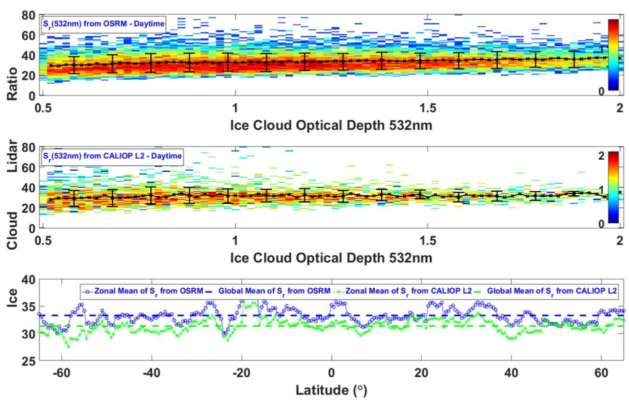

Fig. 3. Upper panel: August 2008 daytime 532 nm Cirrus lidar ratios derived from OSRM. Note that the lidar ratio remains fixed throughout the optical depth ranging from 0.5 to 2. Middle panel: lidar ratios from the corresponding CALIOP V4 L2 cloud layer data. Lower panel: zonal mean distribution of ice cloud lidar ratios. The mean of lidar ratio from OSRM is 33.8 sr (blue line), with a standard deviation of ±4.9 sr, while the mean of CALIOP V4 lidar ratio (green line) is 31.8 sr, with standard deviation of ±4.7 sr.

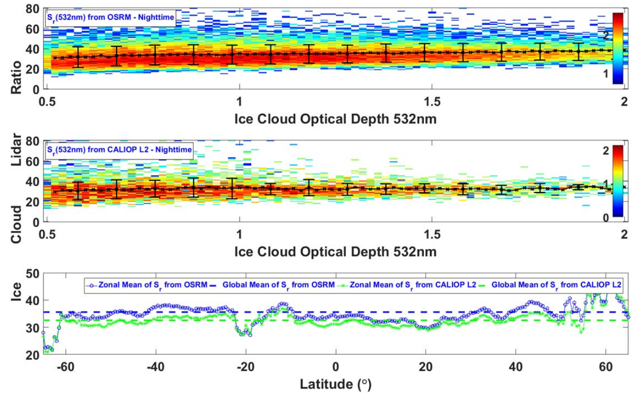

Fig. 4. August 2008 nighttime lidar ratios for 532 nm retrieval results. The mean lidar ratio from OSRM is about 35.3 sr, with a standard deviation of ±4.7 sr, while the mean from CALIOP V4 data is 32.7 sr, with a standard deviation of ±4.3 sr.

(33 ± 5 sr, 31.5 ± 8 sr) with slight variations depending on temperature and latitude, in agreement with our results.

3. RESULTS AND DISCUSSION

In this study, the sea surface is used for accurate estimation of particulate optical depth from CALIOP measurements, since the following information can be easily obtained from either CALIOP or the collocated A-train observations: 1) collocated AMSR-E wind speed data, 2) accurate aerosol free atmosphere information, and 3) improved sea surface backscatter–wind-speed relation with multiple-scattering correction. Several studies ([20,21,23,36]) have used backscatter from the sea surface or other targets to estimate particulate optical depth and calibrate spaceborne lidar.

A. Errors/Uncertainties

The errors/uncertainties can be theoretically assessed from the above equations. From Eq. (11), the relative/fractional uncertainty in γ_{ocean} can be expressed as $\frac{\Delta\gamma_{\text{ocean}}}{\gamma_{\text{ocean}}} \approx -\frac{\Delta\sigma^2}{\sigma^2}$ (higher orders of error terms being ignored). Also, the uncertainty in σ^2 from Eq. (13), $\frac{\Delta\sigma^2}{\sigma^2} \approx \frac{\Delta U}{2U}$ valid for wind speeds of less than 7 m/s, and $\frac{\Delta\sigma^2}{\sigma^2} \approx \frac{\Delta U}{U}$ for wind speeds between 7 and 13.3 m/s, so that $\frac{\Delta\gamma_{\text{ocean}}}{\gamma_{\text{ocean}}} \approx -\frac{\Delta U}{2U}$ for $U < 7$ m/s, and $\frac{\Delta\gamma_{\text{ocean}}}{\gamma_{\text{ocean}}} \approx -\frac{\Delta U}{U}$ for 7 m/s $\leq U < 13.3$ m/s. The uncertainties in wind speed would linearly propagate to sea surface backscatter. For $U < 7$ m/s, a 20% uncertainty in the wind speed is equivalent to a 10% uncertainty in the sea surface backscatter. In the wind speed range 7 m/s $\leq U < 13.3$ m/s, a 10% uncertainty in wind speed is roughly equivalent to about 10% uncertainty in the lidar backscatter. In general, a 1 m/s uncertainty in wind speed is approximately equivalent to about 10% uncertainty in sea surface backscatter, and the resulting uncertainty in particulate optical depth τ_P decreases from 10% to less than 5% for τ_P between 1 and 2.

The three largest sources of uncertainty in the estimation of the optical depth are 1) the uncertainty in AMSR-E wind speed measurements, 2) the uncertainty in lidar calibration, and 3) the estimation of the multiple-scattering effect.

B. Correction for Backscatter due to "Junk"

Figures 5 and 6 demonstrate the importance of correcting for backscatter due to "junk" in the water and subsurface scattering.

As the wind speed increases, the observed ocean surface backscatter γ'_{att} obtained from CALIPSO measurements starts to be dominated by contributions from "junk." The pure ocean surface backscatter estimated from the ocean surface wind speed does not include the influence from whitecaps, bubbles, and foam. After correcting for "junk" backscatter using CALIOP's polarization measurements, a good match is obtained between the backscatter from the ocean surface reflectance model and CALIOP measurements. By comparing the estimated backscatter with measurements, the column optical depth can be obtained. In this paper, we constrain our study to focus solely on the "aerosol-free" sky with single-layer non-water clouds detected by CALIPSO. CALIPSO's level-2 aerosol/cloud layer product is used to ensure that the selected profiles satisfy our purpose. However, as pointed out by others [21], some boundary layer marine aerosols could still remain undetected, since their low altitude combined with their low optical thickness can make them difficult to discriminate from clear air layers using CALIPSO. Josset *et al.* [43] have shown that a positive bias (0.02) can be considered as a systematic error linked to marine boundary layer aerosols, which can be corrected for by a simple subtraction from the total column optical depth. In our study, we take this term into account to ensure a better cirrus optical depth retrieval.

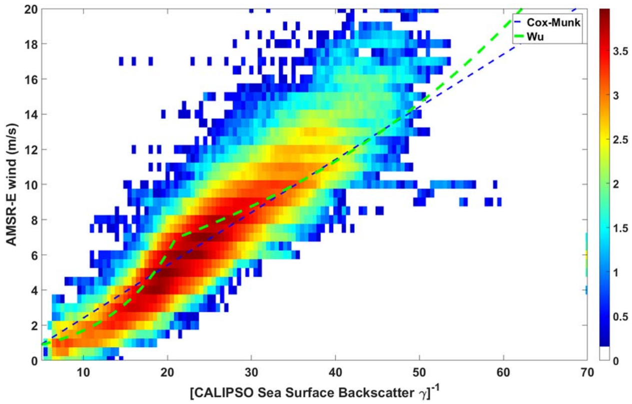

Fig. 5. Relationship between ocean surface wind speed and CALIPSO 532 nm attenuated backscatter. The yellow and green curves are based on the empirical backscatter–wind relations proposed by Cox–Munk and Wu [44]. The underestimate of backscatter from the empirical relations is due to contributions from "junk" in the water and subsurface scattering.

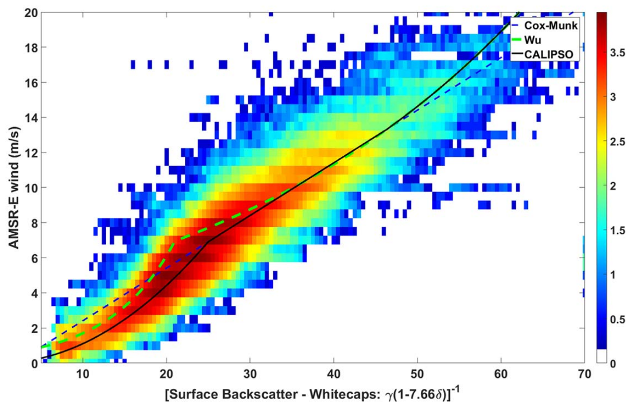

Fig. 6. By correcting CALIPSO observations for "junk" backscatter, a good match is obtained between the backscatter–wind relations and CALIPSO measurements.

C. Comparison of Ice Cloud Optical Depths with CALIPSO Level-2 Data

As a demonstration of the major improvement in the CALIOP V4 optical depths, in Fig. 7 we compare optical depth estimates for semi-transparent ice clouds measured over the ocean during daytime and nighttime, from the collocated OSRM and CALIOP V4 algorithm. In this study, we focus on only the single-layer semi-transparent ice clouds that are detected in the CALIOP 5 km column when minimal aerosol loadings were detected beneath the cirrus layer. These profiles were further restricted by using the extinction QC flags and CAD scores. Data selected by these procedures can be guaranteed

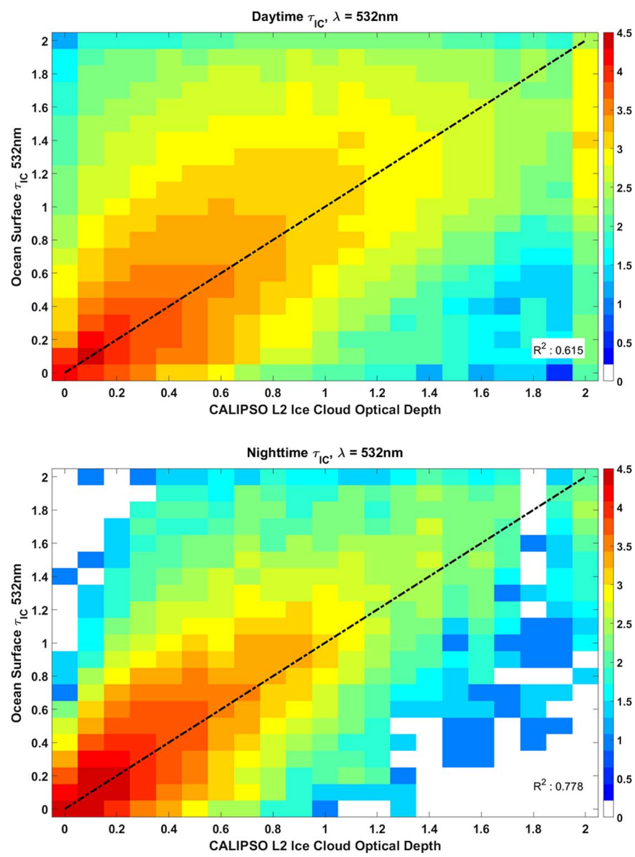

Fig. 7. Comparison of collocated cirrus optical depth from OSRM with that from the CALIOP V4 algorithm from August 2008. Data were sampled over oceans in daytime and between −65°S and 65°N latitude. The color scale indicates number of samples (on $\log_{10}$ scale). Profiles were restricted to cases where there was only one V4 cirrus cloud in the column with no other layer of clouds/aerosols. The upper panel is for daytime, while the bottom panel is for nighttime.

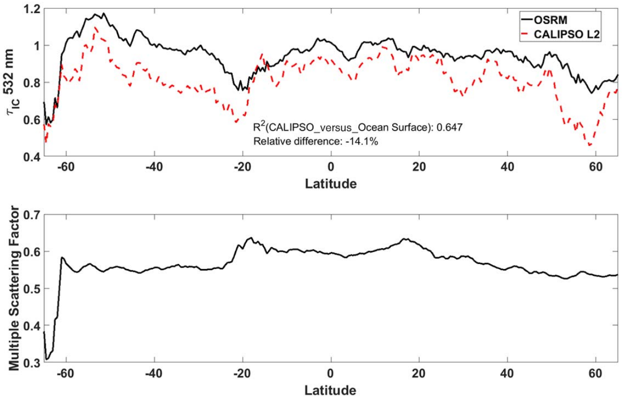

Fig. 8. Upper panel: zonal mean of cirrus optical depth at 532 nm derived from OSRM and CALIPSO V4 L2 data. Lower panel: zonal mean of CALIPSO V4 multiple-scattering factors.

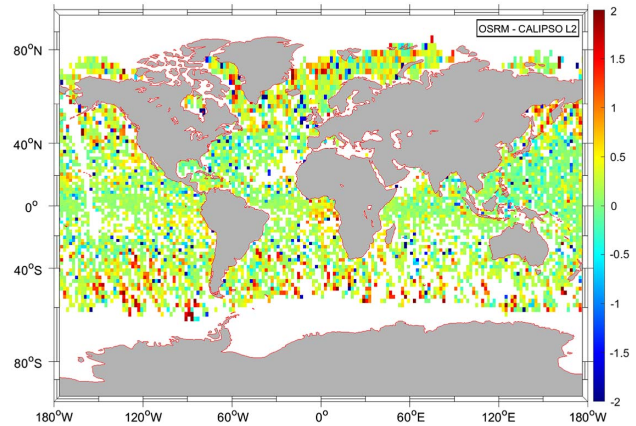

Fig. 10. Difference of cirrus optical depth at 532 nm derived from OSRM and the corresponding CALIPSO V4 level-2 data.

to have high quality and raise the confidence of the comparisons. The comparisons in Fig. 7 show excellent agreement of the V4 optical depths with the OSRM values, with correlation coefficients of 0.615 and 0.778 at daytime and nighttime. The good agreement of the CALIOP V4 and OSRM optical depths gives us confidence to validate the lidar ratios in turn. Comparisons of CALIOP V4 and MODIS C6 optical depths also show that the current CALIOP V4 optical depth is reliable and close to real values [35].

Figure 8 gives the zonal mean of cirrus optical depths from the OSRM and CALIOP V4 algorithms, as well as the zonal mean of the multiple-scattering factor η_P from CALIOP V4 data (daytime+nighttime). The corresponding R^2 coefficient is 0.647, while the relative difference between these two optical depths is 14.1%. The relatively big difference between 50°S and 20°S could be explained by the difference in lidar ratios derived from the OSRM and CALIOP V4 algorithms in the same region. The difference between 50°N and 60°N may be due to few samples being selected in this region. In the area higher than 60°S, the sudden decrease of optical depth of both OSRM and the CALIOP V4 algorithm may be linked to the unusual drop in the multiple-scattering factor.

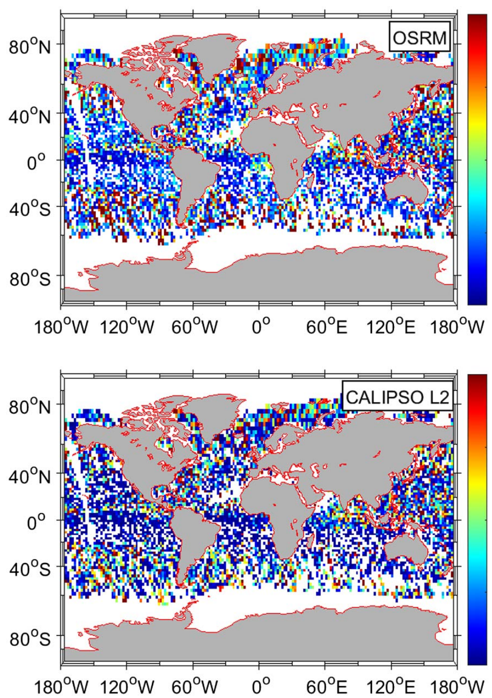

Fig. 9. Upper panel: global distribution of cirrus optical depth at 532 nm derived from OSRM. Lower panel: global distributions of cirrus optical depth at 532 nm from CALIPSO level-2 data. Cirrus optical depths from our OSRM approach generally have the same distribution pattern as the CALIPSO standard V4 product.

Figures 9 and 10 show the global distribution of ice cloud optical depths at 532 nm from OSRM and CALIPSO level 2 data. As can be seen, both datasets have very similar distribution patterns, which ensures our approach is reliable on a global scale. While the patterns of optical depth in other regions agree well, the optical depth derived from CALIPSO underestimated ice cloud optical depths between 30°S and 65°S. This behavior can be linked to the differences in lidar ratios.

The main reasons for the differences are as follows. 1) The temperature and shape dependence of ice cloud lidar ratios in the CALIPSO optical depth retrieval algorithm need further study, implying that uncertainties in the lidar ratio, due to natural variability and misclassification of cloud type, propagate nonlinearly into the estimates of cloud layer optical depth. 2) The "standard" CALIOP cloud retrieval algorithm screens out some cloud layers containing horizontally oriented ice crystals that produced anomalously high specular backscatter from the near nadir-pointing CALIOP beam, implying that reliable extinction estimates cannot be retrieved in these cases [51]. 3) The CALIOP daytime calibration accuracy may still have room for improvement due to the presence of small amounts of aerosols in the atmosphere. 4) Potential bias in the AMSR-E ocean surface wind speeds.

4. CONCLUSION

In this study, we introduced an empirical method that makes use of the perpendicularly polarized signal of the ocean surface to remove the impact of multiple scattering on the retrieved optical depth. This approach may apply to HSRL, which uses molecular backscatter as a target. Since both the ocean surface and molecular backscatter do not lead to depolarization [52], part of the perpendicular component of the ocean surface signal comes from multiple scattering, which causes biases.

We have developed a simple but reliable method to retrieve the ice cloud optical depth from collocated ocean surface wind and lidar backscatter observations. A comparison of optical depths derived by this method with those obtained from CALIPSO standard products shows that the optical depths roughly agree with CALIPSO level-2 data on a global scale. The ice cloud optical depths lie mostly in the range between 0 and 2, and the results from our method are about 14% higher than CALIPSO V4 level-2 data.

In this paper, we optimized the approach to retrieve particulate optical depth from active lidar systems without assuming a lidar ratio for each species of particulates. We also proposed a way to effectively remove the multiply scattered signal at the ocean surface using CALIOP cross-polarization measurements.

The results presented in this paper will allow for improvements in ice cloud discrimination as well as enhancements of CALIPSO extinction profile retrievals and uncertainty estimates.

Funding. NASA CALIPSO Program.

Acknowledgment. The CALIPSO data used in this study were obtained from the NASA Langley Research Center Atmospheric Science Data Center. AMSR data are produced by Remote Sensing Systems and were sponsored by the NASA AMSR-E Science Team and the NASA Earth Science MEaSUREs Program. Data are available at http://www.remss.com.

REFERENCES

1. D. L. Hartmann, J. R. Holton, and Q. Fu, "The heat balance of the tropical tropopause, cirrus, and stratospheric dehydration," Geophys. Res. Lett **28**, 1969–1972 (2001).
2. E. J. Jensen, O. B. Toon, S. A. Vay, J. Ovarlez, R. May, T. Bui, C. Twohy, B. W. Gandrud, R. F. Pueschel, and U. Schumann, "Prevalence of ice-supersaturated regions in the upper troposphere: implications for optically thin ice cloud formation," J. Geophys. Res. **106**, 17253–17266 (2001).
3. D. Atlas, S. Y. Matrosov, A. J. Heymsfield, M.-D. Chou, and D. B. Wolff, "Radar and radiation properties of ice clouds," J. Appl. Meteorol. **34**, 2329–2345 (1995).
4. Q. Yang, Q. Fu, and Y. Hu, "Radiative impacts of clouds in the tropical tropopause layer," J. Geophys. Res. **115**, D00H12 (2010).
5. D. M. Winker, J. Pelon, J. A. Coakley, S. A. Ackerman, R. J. Charlson, P. R. Colarco, P. Flamant, Q. Fu, R. M. Hoff, C. Kittaka, T. L. Kubar, H. Le Treut, M. P. Mccormick, G. Mégie, L. Poole, K. Powell, C. Trepte, M. A. Vaughan, and B. A. Wielicki, "The CALIPSO mission: a global 3D view of aerosols and clouds," Bull. Am. Meteorol. Soc. **91**, 1211–1230 (2010).
6. S. Platnick, M. D. King, S. A. Ackerman, W. P. Menzel, B. A. Baum, J. C. Riedi, and R. A. Frey, "The MODIS cloud products: algorithms and examples from Terra," IEEE Trans. Geosci. Remote Sens. **41**, 459–473 (2003).
7. Z. Zhang, P. Yang, G. Kattawar, J. Riedi, L. Labonnote, B. Baum, S. Platnick, and H.-L. Huang, "Influence of ice particle model on satellite ice cloud retrieval: lessons learned from MODIS and POLDER cloud product comparison," Atmos. Chem. Phys. **9**, 7115–7129 (2009).
8. T. Wang, E. J. Fetzer, S. Wong, B. H. Kahn, and Q. Yue, "Validation of MODIS cloud mask and multilayer flag using CloudSat-CALIPSO cloud profiles and a cross-reference of their cloud classifications," J. Geophys. Res. **121**, 11,620–11,635 (2016).
9. R. Holz, S. Ackerman, F. Nagle, R. Frey, S. Dutcher, R. Kuehn, M. Vaughan, and B. Baum, "Global Moderate Resolution Imaging Spectroradiometer (MODIS) cloud detection and height evaluation using CALIOP," J. Geophys. Res. **113**, D00A19 (2008).
10. J. Joiner, A. Vasilkov, P. Bhartia, G. Wind, S. Platnick, and W. Menzel, "Detection of multi-layer and vertically-extended clouds using A-train sensors," Atmos. Meas. Tech. **3**, 233–247 (2010).
11. J. Delanoë and R. J. Hogan, "Combined CloudSat-CALIPSO-MODIS retrievals of the properties of ice clouds," J. Geophys. Res. **115**, D00H29 (2010).
12. A. Ansmann, M. Riebesell, U. Wandinger, C. Weitkamp, E. Voss, W. Lahmann, and W. Michaelis, "Combined Raman elastic-backscatter lidar for vertical profiling of moisture, aerosol extinction, backscatter, and lidar ratio," Appl. Phys. B **55**, 18–28 (1992).
13. W.-N. Chen, C.-W. Chiang, and J.-B. Nee, "Lidar ratio and depolarization ratio for cirrus clouds," Appl. Opt. **41**, 6470–6476 (2002).
14. D. M. Winker, J. R. Pelon, and M. P. McCormick, "The CALIPSO mission: spaceborne lidar for observation of aerosols and clouds," Proc. SPIE **4893**, 1–11 (2003).
15. Y. Hu, M. Vaughan, Z. Liu, B. Lin, P. Yang, D. Flittner, B. Hunt, R. Kuehn, J. Huang, D. Wu, S. Rodier, K. Powell, C. Trepte, and D. Winker, "The depolarization-attenuated backscatter relation: CALIPSO lidar measurements vs. theory," Opt. Express **15**, 5327–5332 (2007).
16. R. J. Hogan, "Fast approximate calculation of multiply scattered lidar returns," Appl. Opt. **45**, 5984–5992 (2006).
17. H. Okamoto, S. Iwasaki, M. Yasui, H. Horie, H. Kuroiwa, and H. Kumagai, "An algorithm for retrieval of cloud microphysics using 95-GHz cloud radar and lidar," J. Geophys. Res. **108**, 4226 (2003).
18. C. Tinel, J. Testud, J. Pelon, R. J. Hogan, A. Protat, J. Delanoë, and D. Bouniol, "The retrieval of ice-cloud properties from cloud radar and lidar synergy," J. Appl. Meteorol. **44**, 860–875 (2005).
19. J. A. Reagan, X. Wang, and M. T. Osborn, "Spaceborne lidar calibration from cirrus and molecular backscatter returns," IEEE Trans. Geosci. Remote Sens. **40**, 2285–2290 (2002).
20. D. Josset, J. Pelon, A. Protat, and C. Flamant, "New approach to determine aerosol optical depth from combined CALIPSO and CloudSat ocean surface echoes," Geophys. Res. Lett. **35**, L10805 (2008).
21. D. Josset, J. Pelon, A. Garnier, Y. Hu, M. Vaughan, P.-W. Zhai, R. Kuehn, and P. Lucker, "Cirrus optical depth and lidar ratio retrieval from combined CALIPSO-CloudSat observations using ocean surface echo," J. Geophys. Res. **117**, D05207 (2012).
22. J. Reagan and D. Zielinskie, "Spaceborne lidar remote sensing techniques aided by surface returns," Opt. Eng. **30**, 96–103 (1991).
23. S. L. Venkata and J. A. Reagan, "Aerosol retrievals from CALIPSO lidar ocean surface returns," Remote Sens. **8**, 1006 (2016).
24. M. He, Y. Hu, J. P. Huang, and K. Stamnes, "Aerosol optical depth under 'clear' sky conditions derived from sea surface reflection of lidar signals," Opt. Express **24**, A1618–A1634 (2016).
25. F. G. Fernald, B. M. Herman, and J. A. Reagan, "Determination of aerosol height distributions by lidar," J. Appl. Meteorol. **11**, 482–489 (1972).
26. F. G. Fernald, "Analysis of atmospheric lidar observations—some comments," Appl. Opt. **23**, 652–653 (1984).
27. D. M. Winker, M. A. Vaughan, A. Omar, Y. Hu, K. A. Powell, Z. Liu, W. H. Hunt, and S. A. Young, "Overview of the CALIPSO mission and CALIOP data processing algorithms," J. Atmos. Ocean. Technol. **26**, 2310–2323 (2009).
28. J. Kar, M. A. Vaughan, K.-P. Lee, J. L. Tackett, M. A. Avery, A. Garnier, B. J. Getzewich, W. H. Hunt, D. Josset, Z. Liu, P. L. Lucker, B. Magill, A. H. Omar, J. Pelon, R. R. Rogers, T. D. Toth, C. R. Trepte, J.-P. Vernier, D. M. Winker, and S. A. Young, "CALIPSO lidar calibration at 532 nm: version 4 nighttime algorithm," Atmos. Meas. Tech. **11**, 1459–1479 (2018).
29. B. J. Getzewich, M. A. Vaughan, W. H. Hunt, M. A. Avery, K. A. Powell, J. L. Tackett, D. M. Winker, J. Kar, K.-P. Lee, and T. Toth,

"CALIPSO lidar calibration at 532 nm: version 4 daytime algorithm," Atmos. Meas. Tech. **11**, 1459–1479 (2018).
30. A. H. Omar, J.-G. Won, D. M. Winker, S.-C. Yoon, O. Dubovik, and M. P. McCormick, "Development of global aerosol models using cluster analysis of aerosol robotic network (AERONET) measurements," J. Geophys. Res. **110**, D10S14 (2005).
31. G. L. Schuster, M. Vaughan, D. MacDonnell, W. Su, D. Winker, O. Dubovik, T. Lapyonok, and C. Trepte, "Comparison of CALIPSO aerosol optical depth retrievals to AERONET measurements, and a climatology for the lidar ratio of dust," Atmos. Chem. Phys. **12**, 7431–7452 (2012).
32. A. H. Omar, D. M. Winker, J. L. Tackett, D. M. Giles, J. Kar, Z. Liu, M. A. Vaughan, K. A. Powell, and C. R. Trepte, "CALIOP and AERONET aerosol optical depth comparisons: one size fits none," J. Geophys. Res. **118**, 4748–4766 (2013).
33. F. J. S. Lopes, E. Landulfo, and M. A. Vaughan, "Evaluating CALIPSO's 532 nm lidar ratio selection algorithm using AERONET sun photometers in Brazil," Atmos. Meas. Tech. **6**, 3281–3299 (2013).
34. A. Garnier, J. Pelon, M. A. Vaughan, D. M. Winker, C. R. Trepte, and P. Dubuisson, "Lidar multiple scattering factors inferred from CALIPSO lidar and IIR retrievals of semi-transparent cirrus cloud optical depths over oceans," Atmos. Meas. Tech. **8**, 2759–2774 (2015).
35. S. A. Young, M. A. Vaughan, A. Garnier, J. L. Tackett, J. B. Lambeth, and K. A. Powell, "Extinction and optical depth retrievals for CALIPSO's version 4 data release," Atmos. Meas. Tech. **2018**, 1–45 (2018).
36. Y. Hu, K. Stamnes, M. Vaughan, J. Pelon, C. Weimer, D. Wu, M. Cisewski, W. Sun, P. Yang, B. Lin, A. Omar, D. Flittner, C. Hostetler, C. Trepte, D. Winker, G. Gibson, and G. Santa-Maria, "Sea surface wind speed estimation from space-based lidar measurements," Atmos. Chem. Phys. **8**, 3593–3601 (2008).
37. J. L. Bufton, F. E. Hoge, and R. N. Swift, "Airborne measurements of laser backscatter from the ocean surface," Appl. Opt. **22**, 2603–2618 (1983).
38. C. Cox and W. Munk, "Measurement of the roughness of the sea surface from photographs of the sun's glitter," J. Opt. Soc. Am. **44**, 838–850 (1954).
39. C. Cox and W. Munk, *Slopes of the Sea Surface Deduced from Photographs of Sun Glitter* (1956).
40. K. Stamnes and J. J. Stamnes, *Radiative Transfer in Coupled Environmental Systems: An Introduction to Forward and Inverse Modeling* (Wiley, 2016).
41. Y. Liu, X.-H. Yan, W. T. Liu, and P. A. Hwang, "The probability density function of ocean surface slopes and its effects on radar backscatter," J. Phys. Oceanogr. **27**, 782–797 (1997).
42. A. H. Monahan, "The probability distribution of sea surface wind speeds. Part I: theory and seawinds observations," J. Clim. **19**, 497–520 (2006).
43. D. Josset, P.-W. Zhai, Y. Hu, J. Pelon, and P. L. Lucker, "Lidar equation for ocean surface and subsurface," Opt. Express **18**, 20862–20875 (2010).
44. J. Wu, "Mean square slopes of the wind-disturbed water surface, their magnitude, directionality, and composition," Radio Sci. **25**, 37–48 (1990).
45. M. A. Bourassa, R. Romero, S. R. Smith, and J. J. O'Brien, "A new FSU winds climatology," J. Clim. **18**, 3686–3698 (2005).
46. F. J. Wentz and T. Meissner, "AMSR ocean algorithm theoretical basis document, version 2," RSS Tech. Proposal 121599A-1 (Remote Sensing Systems, 2000).
47. H.-M. Zhang, J. J. Bates, and R. W. Reynolds, "Assessment of composite global sampling: sea surface wind speed," Geophys. Res. Lett. **33**, L17714 (2006).
48. N. Ebuchi, H. C. Graber, and M. J. Caruso, "Evaluation of wind vectors observed by QuikSCAT/SeaWinds using ocean buoy data," J. Atmos. Ocean. Technol. **19**, 2049–2062 (2002).
49. C. M. R. Platt, "Lidar and radiometric observations of cirrus clouds," J. Atmos. Sci. **30**, 1191–1204 (1973).
50. C. M. R. Platt, S. A. Young, R. T. Austin, G. R. Patterson, D. L. Mitchell, and S. D. Miller, "LIRAD observations of tropical cirrus clouds in MCTEX. Part I: optical properties and detection of small particles in cold cirrus," J. Atmos. Sci. **59**, 3145–3162 (2002).
51. M. Avery, D. Winker, A. Heymsfield, M. Vaughan, S. Young, Y. Hu, and C. Trepte, "Cloud ice water content retrieved from the CALIOP space-based lidar," Geophys. Res. Lett. **39**, L05808 (2012).
52. W. H. Hunt, D. M. Winker, M. A. Vaughan, K. A. Powell, P. L. Lucker, and C. Weimer, "CALIPSO lidar description and performance assessment," J. Atmos. Ocean. Technol. **26**, 1214–1228 (2009).